Investigation of Pulsating Vector Excitation Saliency-based Rotor Position Estimation Method in Current-Source Inverters

Renato Amorim Torres[1], Hang Dai[1], Woongkul Lee[2], Thomas Jahns[1], Bulent Sarlioglu[1]
[1] University of Wisconsin-Madison, United States
[2] Michigan State University, United States

***Abstract*-- While many self-sensing (sensorless) control methods have been developed for voltage source inverters (VSIs), there has been limited investigation into how these methods perform with current-source inverter (CSI) drives, which are becoming more attractive with recent advances in monolithic four-quadrant switches. This paper presents a pulsating vector excitation saliency-based rotor position estimation method that can be adapted for CSI-based motor drives. The benefits of using CSIs are discussed, including improved voltage measurement accuracy and compatibility with low-inductance machines. This paper explains how to tailor the pulsating vector excitation saliency-based method for CSI-based motor drives, with a focus on the important issues of capacitor unbalance effects and CSI-load resonances. A detailed mathematical model for the rotor position estimation method is provided, together with experimental verification results.**

***Index Terms* — current-source inverter, high-frequency injection, pulsating vector excitation, rotor position estimation, self-sensing, sensorless.**

I. Introduction

Self-sensing rotor position estimation techniques, often referred to as sensorless control, make it possible to eliminate the angular position sensor (such as encoders and resolvers) from motor drives. These methods are attractive for several applications since they reduce the motor drive's overall cost and volume, increase the drive system's reliability, and improve its manufacturability.

Despite the extensive research in rotor position sensor elimination techniques reported to date, the vast majority are designed for voltage-source inverter (VSI)-based motor drives due to its dominance that resulted from the ascendance of superior silicon-based insulated-gate bipolar transistors (IGBTs) and power metal–oxide–semiconductor field-effect transistors (MOSFETs) during the 1980s and 1990s [1]. Since IGBTs and power MOSFETs generally have poor or non-existent reverse-voltage-blocking (RVB) capability that is required by current-source inverters (CSIs), the CSI topology gave way during 1990s to the VSI for the large majority of new ASDs, except for megawatt-class medium-voltage inverters, which continued to use thyristor-based CSIs [1].

Recent advances in the development of monolithic four-quadrant (FQ) switches with RVB capabilities are now offering appealing switch candidates for use in CSIs. More specifically, these new monolithic devices reduce the switch conduction losses significantly compared to series combinations of MOSFETs and series diodes that have typically been adopted to provide the required reverse-voltage blocking capability. For example, the development of a monolithic silicon carbide (SiC)-based bidirectional power switch device with RVB capability is reported in [2]. These new devices are appealing for a variety of power converter topologies that need RVB switches, including matrix inverters and CSIs [2].

Recent research has highlighted some of the appealing advantages that CSIs can offer compared to traditional VSIs, particularly when combined with the ultra-fast switching capabilities of wide-bandgap (WBG) switches. These advantage include the CSI's quasi-sinusoidal output voltage waveforms that significantly reduce the voltage stress on machine windings, resulting in increased reliability, lifetime, and improved machine power density due to thinner winding insulation requirements [3].

In contrast to VSIs, CSIs have improved compatibility with low-inductance machines due to the dc link inductor that lies at the heart of every CSI combined with its output capacitors. Exciting a low-inductance machine with a VSI can lead to excessive phase current ripple, resulting in elevated machine losses and torque ripple. In contrast, the CSI's output capacitors provide additional filtering of the inverter PWM switching harmonics, dramatically reducing the machine's stator current ripple even for machines with very low machine inductances. Although the topic is not explored in this paper, low machine inductance helps reduce the sensitivity of model-based back-emf rotor position estimation sensitive to the current measurement accuracy [4]. Therefore, the improved compatibility of CSIs with low-inductance machines opens a promising pathway to improved accuracy of model-based rotor position estimation accuracy compared to VSI-based motor drives.

The extensive reported research on rotor position sensor elimination techniques reported to date has been primarily focused on their implementation with VSI drives. These works provide very little insight into how these techniques perform in CSI-based drives and what modifications are required to obtain the best possible performance. As discussed later, there are noticeable differences between the implementation of self-sensing techniques due to VSI and CSI's topology differences. A few papers have reported investigations of self-sensing techniques for CSIs

[4]–[17]. Those works are generally limited to induction machines or thyristor-based drives that severely limit the motor drive switching frequency and control bandwidth. Additionally, most of these papers do not provide a comprehensive approach that includes practical implementation issues, such as the possibility of unbalanced output filter capacitors.

Among the CSI-based references that investigate self-sensing techniques for synchronous motor (SM) drives, most of them present techniques suitable for mid- to high-speed range based on back-EMF estimation. Only one reference [14] has been found in the literature that investigates the adoption of high-frequency injection (HFI) to achieve low-speed operation in current-source-fed permanent magnet (PM) motor drives. Even though this work lays the foundation for achieving low-speed operation of self-sensing position estimation using current source-fed drives, its focus on silicon-based inverters with low switching frequencies limit its applicability to CSIs using new generation of WBG power devices. For example, the adoption of thyristor-based inverters in [15] limited the maximum value of the injected signal to a very low value of only 300 Hz.

The objective of this paper is to investigate self-sensing position estimation in CSIs with high switching frequencies using the pulsating vector excitation (PVE) saliency-based rotor position estimation method. Attention is particularly focused on machine operation at static and low speeds using PM synchronous machines. The paper structure is summarized as follows. The second section provides a detailed explanation of the PVE saliency-based rotor position estimation method in current-source inverters. The third section presents important aspects to consider when selecting the frequency of the high-frequency injected signal. The fourth section explores the effect of unbalanced output capacitors on the performance of the rotor position estimation. Experimental results are provided in the fifth section that support the presented analytical results. Finally, the major conclusions from the paper concerning the application of self-sensing techniques in CSI-based motor drives are presented in the final (sixth) section.

II. Pulsating Vector Excitation Saliency-Based Rotor Position Estimation Method

The pulsating vector excitation (PVE) saliency-based rotor position estimation method used in VSI-based motor drives [18] can be adapted to CSI-based motor drives. However, some topological differences, such as the presence of output filter capacitors, must be considered. This section explains how to tailor the PVE saliency-based method for CSI-based motor drives, investigating and analyzing aspects such as capacitor unbalance and CSI-load resonance.

The set of equations (1) describes the dynamics of a PM synchronous machine and the CSI output filter capacitor in the synchronous reference frame. The synchronous reference frame is represented by the superscript e. The subscripts d and q represent d- and q-axis components. Therefore, v_d^e, v_q^e, $i_{s,d}^e$, $i_{s,q}^e$, $i_{c,d}^e$, $i_{c,q}^e$, L_d and L_q corresponds respectively to the d- and q-axis components of the machine terminal voltage, machine stator currents, output capacitors currents, and machine inductance. R_s corresponds to the machine stator resistance, C is CSI output filter capacitance, ω_r is the electrical angular speed, λ_{PM} is the PM flux linkage and p represents the derivative operator. It is assumed that the CSI output capacitors are balanced for these equations.

$$\begin{bmatrix} v_d^e \\ v_q^e \end{bmatrix} = \begin{bmatrix} R_s + L_d p & -\omega_r L_q \\ \omega_r L_d & R_s + L_q p \end{bmatrix} \begin{bmatrix} i_{s,d}^e \\ i_{s,q}^e \end{bmatrix} + \begin{bmatrix} 0 \\ \omega_r \lambda_{PM} \end{bmatrix}$$
$$p \begin{bmatrix} v_d^e \\ v_q^e \end{bmatrix} = \begin{bmatrix} 0 & \omega_r \\ -\omega_r & 0 \end{bmatrix} \begin{bmatrix} v_d^e \\ v_q^e \end{bmatrix} + \begin{bmatrix} 1/C & 0 \\ 0 & 1/C \end{bmatrix} \begin{bmatrix} i_{c,d}^e \\ i_{c,q}^e \end{bmatrix} \quad (1)$$

Assuming that the injected signal frequency is high, and the machine is operating at a low speed, the speed-dependent terms in (1) can be neglected. As a result, (1) simplifies to (2), where the subscript h refers to the high-frequency components and steady-state operation is assumed ($p = j\omega_h$). Note that the voltage and current variables in (2) are phasors and denoted using capitalized bold variable names with a tilde accent (e.g., $\tilde{\boldsymbol{X}} = a + jb$). The impedances are complex numbers denoted using uppercase bold variable names (e.g., $\boldsymbol{X} = a + jb$). It should be noted that the conversion from the phasors to the steady-state time domain is given by $x(t) = Re\{\tilde{X}e^{j\omega_h t}\}$.

$$\begin{bmatrix} \tilde{\boldsymbol{V}}_{dh}^e \\ \tilde{\boldsymbol{V}}_{qh}^e \end{bmatrix} = \begin{bmatrix} \boldsymbol{Z}_{dh} & 0 \\ 0 & \boldsymbol{Z}_{qh} \end{bmatrix} \begin{bmatrix} \tilde{\boldsymbol{I}}_{dh}^e \\ \tilde{\boldsymbol{I}}_{qh}^e \end{bmatrix} = \begin{bmatrix} \dfrac{R_{sh} + j\omega_h L_{dh}}{1 + j\omega_h R_{sh} C_h - \omega_h^2 L_{dh} C_h} & 0 \\ 0 & \dfrac{R_{sh} + j\omega_h L_{qh}}{1 + j\omega_h R_{sh} C_h - \omega_h^2 L_{qh} C_h} \end{bmatrix} \begin{bmatrix} \tilde{\boldsymbol{I}}_{dh}^e \\ \tilde{\boldsymbol{I}}_{qh}^e \end{bmatrix} \quad (2)$$

The voltage and current phasors of (2) can be translated to the estimated reference frame (superscript $\hat{e}$) using the relation $\boldsymbol{x}^e = T(\theta_{err})\boldsymbol{x}^{\hat{e}}$, where $T(\theta_{err})$ is the transformation matrix that rotates the synchronous reference frame by θ_{err}. θ_{err} corresponds to the error angle between the actual rotor position θ_r (electrical angle) and the estimated rotor position $\hat{\theta}_r$ (electrical angle) as represented in Fig. 1. Applying this error angle

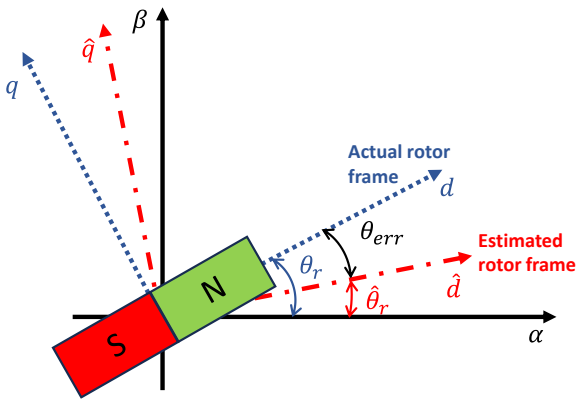

Fig. 1: Vector representation of the pulsating vector excitation method error angle θ_{err} between the actual rotor position θ_r and the estimated rotor position $\hat{\theta}_r$.

definition to the voltages and currents in (2) leads to the following expression for the high-frequency components in the estimated synchronous reference frame:

$$\begin{bmatrix}\tilde{\boldsymbol{V}}_{dh}^{\hat{e}}\\ \tilde{\boldsymbol{V}}_{qh}^{\hat{e}}\end{bmatrix} = T^{-1}(\theta_{err})\begin{bmatrix}\boldsymbol{Z}_{dh} & 0\\ 0 & \boldsymbol{Z}_{qh}\end{bmatrix} T(\theta_{err})\begin{bmatrix}\tilde{\boldsymbol{I}}_{dh}^{\hat{e}}\\ \tilde{\boldsymbol{I}}_{qh}^{\hat{e}}\end{bmatrix} = \begin{bmatrix}\boldsymbol{Z}_{avg} - \boldsymbol{Z}_{diff}\cos(2\theta_{err}) & -\boldsymbol{Z}_{diff}\sin(2\theta_{err})\\ -\boldsymbol{Z}_{diff}\sin(2\theta_{err}) & \boldsymbol{Z}_{avg} + \boldsymbol{Z}_{diff}\cos(2\theta_{err})\end{bmatrix}\begin{bmatrix}\tilde{\boldsymbol{I}}_{dh}^{\hat{e}}\\ \tilde{\boldsymbol{I}}_{qh}^{\hat{e}}\end{bmatrix} \quad (3)$$

where

$$\theta_{err} \triangleq \theta_r - \widehat{\theta_r} \rightarrow T(\theta_{err}) = \begin{bmatrix}\cos(\theta_{err}) & \sin(\theta_{err})\\ -\sin(\theta_{err}) & \cos(\theta_{err})\end{bmatrix}$$

$$\boldsymbol{Z}_{avg} \triangleq \frac{\boldsymbol{Z}_{dh} + \boldsymbol{Z}_{qh}}{2}, \quad \boldsymbol{Z}_{diff} \triangleq \frac{\boldsymbol{Z}_{qh} - \boldsymbol{Z}_{dh}}{2}$$

If the high-frequency injected current is only applied in the d-axis, as shown in (4), the simplified d- and q-axis voltages can be expressed as shown in (5).

$$\begin{aligned} i_{dh}^{\hat{e}} &= I_{inj}\cos(\omega_h t) \rightarrow \tilde{\boldsymbol{I}}_{dh}^{\hat{e}} = I_{inj}\\ i_{qh}^{\hat{e}} &= 0 \rightarrow \tilde{\boldsymbol{I}}_{qh}^{\hat{e}} = 0 \end{aligned} \quad (4)$$

$$\begin{aligned} \tilde{\boldsymbol{V}}_{dh}^{\hat{e}} &= I_{inj}\left(\boldsymbol{Z}_{avg} - \boldsymbol{Z}_{diff}\cos 2\theta_{err}\right)\\ \tilde{\boldsymbol{V}}_{qh}^{\hat{e}} &= I_{inj}\left(-\boldsymbol{Z}_{diff}\sin 2\theta_{err}\right) \end{aligned} \quad (5)$$

Notice from (5) that the quadrature voltage component in the estimated reference frame $\tilde{\boldsymbol{V}}_{qh}^{\hat{e}}$ is zero when the rotor position error θ_{err} is zero. Therefore, a control loop can be designed to minimize θ_{err}, where the feedback is based on the measured quadrature voltage $v_{qh}^{\hat{e}}$. This control loop is shown in Fig. 2, where the concept of demodulation is used, as shown inside the red dashed-line box. Fig. 2 will be explained in detail next.

Let us assume that the signal $v_q^{\hat{e}}$ has a high-frequency quadrature voltage component in the format $v_{qh}^{\hat{e}} = A\cos(\omega_h t + \phi_{hq})$. By multiplying $v_{qh}^{\hat{e}}$ by a high-frequency demodulating cosine wave $\cos(\omega_h t + \phi_{dem})$, the signal δ (identified in the block diagram of Fig. 2) is generated. The signal δ has two components: a dc component and a high-frequency component, as shown in (6). The high-frequency component will be filtered out uisng the low-pass filter (LPF), and the remaining dc component will be used to extract the position estimation. Therefore, maximizing the dc-component is beneficial for improving the signal-to-noise ratio (SNR). From (6), it can be seen that, for a fixed signal amplitude A, the dc-component is maximized when $\phi_{dem} = \phi_{hq}$.

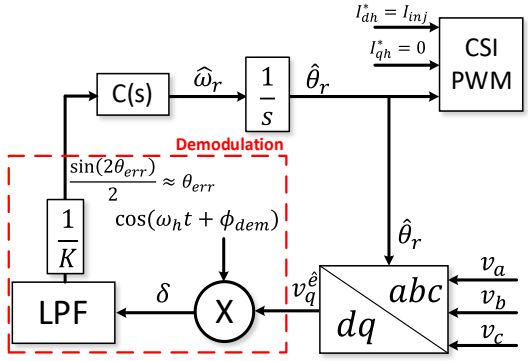

Fig. 2: Control block diagram of a closed-loop system for a PVE scheme for rotor angle self-sensing that minimizes angle error $\boldsymbol{\theta_{err}}$ between real rotor position $\boldsymbol{\theta_r}$ and estimated rotor position $\boldsymbol{\hat{\theta}_r}$.

$$\begin{aligned} \delta &= v_{qh}^{\hat{e}} \cdot \cos(\omega_h t + \phi_{dem})\\ &= A\cos(\omega_h t + \phi_{hq}) \cdot \cos(\omega_h t + \phi_{dem})\\ &= A\left(\frac{\cos(\phi_{hq} - \phi_{dem})}{2} + \frac{\cos(2\omega_h t + \phi_{hq} + \phi_{dem})}{2}\right) \end{aligned} \quad (6)$$

From (5), the signal $v_{qh}^{\hat{e}}$ can be represented by a phasor of magnitude A and phase ϕ_{hq} (i.e., $\tilde{\boldsymbol{V}}_{qh}^{\hat{e}} \triangleq A\angle\phi_{hq}$), where $A = -I_{inj} \cdot |\boldsymbol{Z}_{diff}| \cdot sin2\theta_{err}$ and $\phi_{hq} = \angle\boldsymbol{Z}_{diff}$. Using (6) and setting the phase of the demodulating cosine wave to $\phi_{dem} = \phi_{hq}$ yields:

$$\delta = \frac{A}{2} + \frac{\cos(2\omega_h t + 2\theta_{hq})}{2} \quad (7)$$

where
$A = -I_{inj} \cdot |\boldsymbol{Z}_{diff}| \cdot sin2\theta_{err}$ and $\phi_{hq} = \angle\boldsymbol{Z}_{diff}$

By applying a low-pass filter to the signal δ, (8) is obtained.

$$LPF\{\delta\} = \frac{A}{2} = -|\boldsymbol{Z}_{diff}|I_{inj}\frac{sin2\theta_{err}}{2} \quad (8)$$

Once the position estimator converges and is tracking the actual rotor position, it can be assumed that θ_{err} is approximately zero; therefore, $\sin(2\theta_{err}) \approx 2\theta_{err}$. Thus, the estimated rotor position angle error θ_{err} can be estimated by dividing the result of (8) by the constant K, as shown in (9).

$$\frac{LPF\{\delta\}}{K} \approx \theta_{err}, \text{ where } K = -|\boldsymbol{Z}_{diff}|I_{inj} \quad (9)$$

At this point, a critical observation must be made. As mentioned before, the demodulation cosine waveform's phase angle ϕ_{dem} should be equal to ϕ_{hq} to maximize the dc component of signal δ, which is ultimately used for extracting the rotor position estimation error. The angle ϕ_{hq} corresponds to the angle of the impedance difference between d- and q-axis ($\phi_{hq} = \angle\boldsymbol{Z}_{diff}$). As will be shown later, the closer the frequency of the injected signal is to the d- or q-axis resonant frequencies, the higher the impedance difference $\boldsymbol{Z}_{diff}$. Since a higher impedance difference is beneficial for improving the SNR of the estimated rotor position, it can be advantageous to inject signals with frequencies close to the resonance. However, the angle of the impedance difference also changes quickly as the injected signal frequency approaches one of the resonant frequencies; thus, it is important to correct the phase of the demodulating cosine wave by setting $\phi_{dem} = \phi_{hq}$ to extract the maximum benefit of injecting signals close to the resonant frequencies. This aspect has not been previously reported in the literature.

III. Frequency Selection of High-Frequency Injected Signal

Table 1 shows the CSI-SPM motor drive parameters used throughout the subsequent analysis.

Table 1: CSI-SPM Motor Drive System Parameters

Parameters	Symbol	Value
Machine model	-	AKM2G-72P
Output filter phase capacitance	C	2.2 μF
Machine high-frequency d-axis inductance	L_{dh}	3.65 mH
Machine high-frequency q-axis inductance	L_{qh}	4.07 mH
Saliency ratio	L_{qh}/L_{dh}	1.115
Machine phase resistance	R_s	0.1575 Ω
Machine pole pairs	P	4
Machine torque constant	K_t	1.93 Nm/Arms
Maximum torque current	I_{MAX}	8.5Arms
Total system inertia	I	0.04 Kg m^2
Permanent magnet flux linkage	λ_{PM}	0.2515 V·s
Switching/Sampling frequency	f_s	70 kHz
Voltage sensor analog filter cutoff frequency	$f_{c,v}$	30 kHz
Current sensor analog filter cutoff frequency	$f_{c,i}$	30 kHz

Different factors must be considered when selecting the frequency of the injected signal, such as losses, SNR ratio, modulation index allocation, bandwidth, and distortions due to unbalanced output capacitors. The combination of the output capacitor and the machine inductances creates resonant circuits. Care must be taken to prevent the high-frequency injected signal from heavily exciting these resonant frequencies which would induce high currents in the machine and output capacitors, potentially damaging the drive due to excessive losses or overvoltage. Nevertheless, injecting the high-frequency signal at a frequency close to the resonant frequency can be advantageous. The first advantage is the amplification of the high-frequency injected signal [19], where a minimal current injected by the CSI can drive large currents and voltages across the CSI output capacitors and machine terminals. This property enables allocating a small portion of the CSI dc-link current towards the high-frequency injection. Even the amplification gain can be regulated in real-time by modifying the frequency of the injected signal.

It can be seen from (7) that the signal δ, which is ultimately used for extracting the rotor position estimation, is proportional to the magnitude of the impedance difference between d- and q-axis $|\boldsymbol{Z}_{diff}|$.Therefore, a higher $|\boldsymbol{Z}_{diff}|$ improves the SNR of the estimated rotor position. Fig. 3 shows the value of $|\boldsymbol{Z}_{diff}|$ in the CSI system investigated for different frequencies. Notice that this value peaks at either the d-axis or q-axis resonant frequencies (1776 Hz and 1682 Hz, respectively). Additionally, $|\boldsymbol{Z}_{diff}|$ drops sharply for frequencies away from both resonant frequencies.

Fig. 4 shows simulation results comparing the SNR ratio of the rotor position estimation for different injected signal frequencies, namely 700 Hz, 1000 Hz, and 1500 Hz. The simulation included different aspects of the power electronics, such as voltage drop across switching devices, overlap time, and sensor dynamics. A voltage-behind

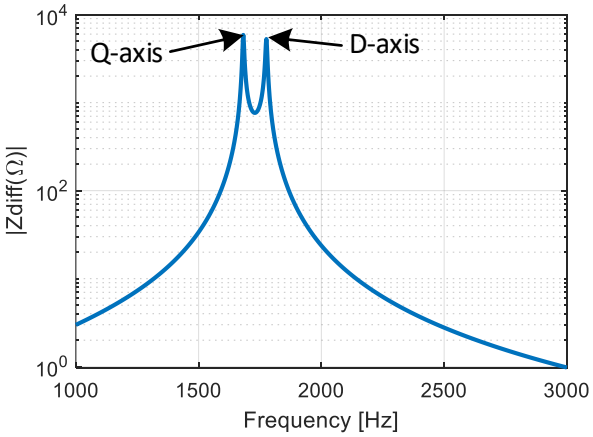

Fig. 3: Calculated magnitude of the impedance difference between the d- and q-axes ($\boldsymbol{Z}_{diff}$) plotted as a function of the frequency of the injected signal.

reactance salient PM machine model is used in a torque-mode operation. Magnetic saturation effects were disregarded. Band-limited white noise was injected into the voltage and current signals for evaluation of the SNR of the rotor position estimation.

The SNR was calculated using (10). It should be noted that the estimated rotor position is converted into a sinusoidal signal as $\sin(\hat{\theta}_{est})$ in order to evaluate the SNR using (10). The simulation results confirm that operation closer to the resonant frequency improves the SNR. For example, the SNR value when injecting the signal at 1500 Hz is 26.6 dB higher than an injection at 700 Hz. This result is somewhat expected since the high-frequency voltage signal response amplitude, which is used for extracting the rotor position information, increases at frequencies closer to the resonant frequencies.

$$SNR_{DB} = 10\log_{10}\left(\frac{P_{signal}}{P_{noise}}\right) = 10\log_{10}\left(\frac{RMS_{signal}}{RMS_{noise}}\right)^2 \quad (10)$$

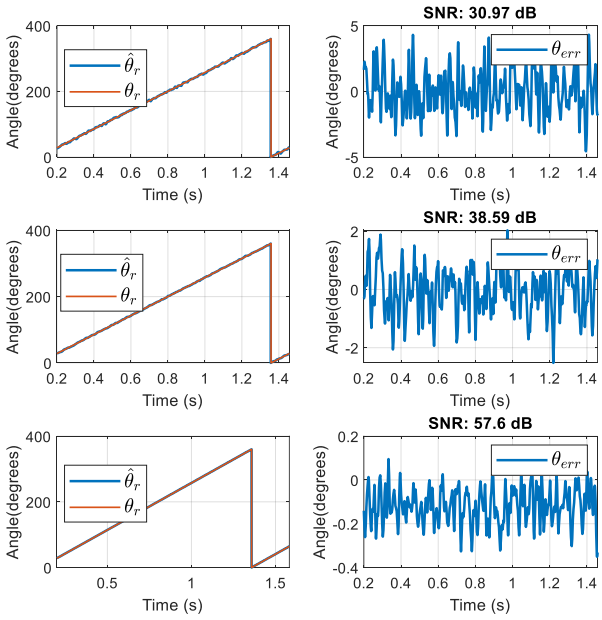

Fig. 4: Simulation results comparing the SNR ratio of the rotor position estimation for different injected signal frequencies: (top) 700 Hz; (middle) 1000 Hz; and (bottom) 1500 Hz.

$$\begin{bmatrix}\tilde{\boldsymbol{V}}^{\hat{e}}_{dh}\\ \tilde{\boldsymbol{V}}^{\hat{e}}_{qh}\end{bmatrix} = T^{-1}(\theta_{err})\begin{bmatrix}\boldsymbol{Z}_{dh} & \boldsymbol{Z}_{dqh}\\ \boldsymbol{Z}_{dqh} & \boldsymbol{Z}_{qh}\end{bmatrix}T(\theta_{err})\begin{bmatrix}\tilde{\boldsymbol{I}}^{\hat{e}}_{dh}\\ \tilde{\boldsymbol{I}}^{\hat{e}}_{qh}\end{bmatrix} = \begin{bmatrix}\boldsymbol{Z}_{avg} - \boldsymbol{Z}_{diff}\cos(2\theta_{err}) & \boldsymbol{Z}_{dqh}\cos(2\theta_{err}) - \boldsymbol{Z}_{diff}\sin(2\theta_{err})\\ \boldsymbol{Z}_{dqh}\cos(2\theta_{err}) - \boldsymbol{Z}_{diff}\sin(2\theta_{err}) & \boldsymbol{Z}_{avg} + \boldsymbol{Z}_{diff}\cos(2\theta_{err})\end{bmatrix}\begin{bmatrix}\tilde{\boldsymbol{I}}^{\hat{e}}_{dh}\\ \tilde{\boldsymbol{I}}^{\hat{e}}_{qh}\end{bmatrix} \quad (11)$$

IV. Effects of Unbalanced CSI Output Capacitors

Although the CSI enables amplification of the injected signal by leveraging the resonant circuit, the presence of the output filter capacitors can introduce undesirable disturbances that must be better understood. The first aspect investigated is the perturbation on the rotor position estimation by a potential unbalance of the CSI's output filter capacitors and the resulting sensitivity of the rotor position estimation accuracy to any such unbalance.

In the preceding section, the impedance matrix terms Z_{12} and Z_{21} in (2) are zero. These null terms are a consequence of a three-phase balanced system with no cross-coupling between the *d*- and *q*-axes of the machine. The authors of [20] investigated the effect of cross-coupled magnetic saturation on the performance of a saliency-based rotor position estimation method. They reported that the terms Z_{12} and Z_{21} become non-zero ($Z_{12} = Z_{21} \neq 0$) as a result of cross-coupled magnetic saturation. A similar effect occurs in the presence of unbalanced output capacitors; however, in this case, the cross-coupling terms are not constant and vary with the rotor position.

Fig. 5(a) shows the values of the impedances $\boldsymbol{Z}_{dh}$, $\boldsymbol{Z}_{qh}$ and $\boldsymbol{Z}_{dqh}$ for the drive under investigation at different rotor positions (from 0 to 360° electrical) assuming balanced output capacitors. The results show that the three impedances are constant and $\boldsymbol{Z}_{dqh}$ is zero for balanced conditions. Figs. 5(b) and 5(c) show the same plot for unbalanced output capacitors ($C_a = 1.1C, C_b = C, C_c = 0.9C$). in this case, $\boldsymbol{Z}_{dh}$, $\boldsymbol{Z}_{qh}$ and $\boldsymbol{Z}_{dqh}$ are no longer constant and $\boldsymbol{Z}_{dqh}$ takes on non-zero values.

Equation (11) shows the results of applying the same procedure used to derive (3) except that the cross-coupling impedance terms (i.e., $Z_{12} = Z_{21} = \boldsymbol{Z}_{dqh}$) are now non-zero. It should be noted in the last equation of (11) that the off-diagonal terms now have an additional component of $\boldsymbol{Z}_{dqh}\cos(2\theta_{err})$, which was not present in (3). This component represents a disturbance input for the saliency-based self-sensing algorithm.

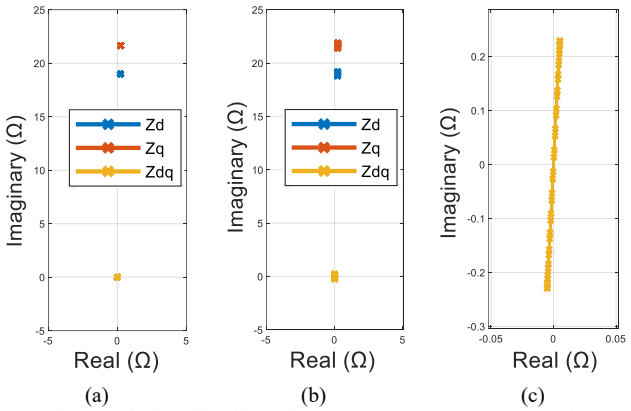

Fig. 5: Calculated load impedances $\boldsymbol{Z}_{dh}$, $\boldsymbol{Z}_{qh}$ and $\boldsymbol{Z}_{dqh}$ of the investigated CSI motor drive for different rotor positions (from 0 to **360°** electrical) assuming: (a) balanced output capacitors, and (b) unbalanced output capacitors ($\boldsymbol{C_a = 1.1C, C_b = C, C_c = 0.9C}$). (c) Zoomed plot of (b) around the origin.

Since the PVE strategy is unmodified, (6) remains valid and the signal $v^{\hat{e}}_{qh}$ can still be represented by a phasor of magnitude A and phase ϕ_{hq} ($\tilde{\boldsymbol{V}}^{\hat{e}}_{qh} \triangleq A\angle\phi_{hq}$). However, the amplitude and phase of $v^{\hat{e}}_{qh}$ are now given by: $A = I_{inj}\cdot|\boldsymbol{Z}_{dqh}\cos(2\theta_{err}) - \boldsymbol{Z}_{diff}\sin(2\theta_{err})|$ and $\phi_{hq} = \angle\left(\boldsymbol{Z}_{dqh}\cos(2\theta_{err}) - \boldsymbol{Z}_{diff}\sin(2\theta_{err})\right)$. The injected signals are the same as for the balanced capacitance case; $\tilde{\boldsymbol{I}}^{\hat{e}}_{dh} = I_{inj}$ and $\tilde{\boldsymbol{I}}^{\hat{e}}_{qh} = 0$.

As shown in the preceding section, the PVE self-sensing algorithm is designed to regulate the estimated rotor position $\hat{\theta}_r$ by using a feedback loop to drive $\tilde{\boldsymbol{V}}^{\hat{e}}_{qh}$ to zero. In an ideally balanced system, this is achieved when the cross-coupling term $-\boldsymbol{Z}_{diff}\sin(2\theta_{err})$ in (3) equals zero, which translates into θ_{err} being zero. However, in (11), the cross-coupling term is $\boldsymbol{Z}_{dqh}\cos(2\theta_{err}) - \boldsymbol{Z}_{diff}\sin(2\theta_{err})$, and no angle θ_{err} satisfies the identity $\boldsymbol{Z}_{dqh}\cos(2\theta_{err}) - \boldsymbol{Z}_{diff}\sin(2\theta_{err}) = 0$ since $\boldsymbol{Z}_{dqh}$ and $\boldsymbol{Z}_{diff}$ are not collinear complex numbers. Nevertheless, the PVE control loop will do its best to continuously minimize $\tilde{\boldsymbol{V}}^{\hat{e}}_{qh}$ despite the unbalance.

Fig. 6 shows the value of $|\tilde{\boldsymbol{V}}^{\hat{e}}_{qh}|$ calculated via (11) for different estimated rotor position values $\hat{\theta}_r$ when the rotor is static at $\theta_r = 0$. The results show that the minimal value of $|\tilde{\boldsymbol{V}}^{\hat{e}}_{qh}|$ occurs when $\hat{\theta}_r = 3.19°$ (i.e., $\theta_{err} = -3.19°$). This angle corresponds to the same rotor position estimation angle obtained via simulation of the PVE self-sensing algorithm under the same unbalanced capacitor conditions.

As noted previously and shown in Figs. 5(b) and 5(c), the complex value of $\boldsymbol{Z}_{dqh}$ varies for different rotor positions. This complex value of $\boldsymbol{Z}_{dqh}$ completes two full cycles within a single full rotor electrical cycle (i.e., twice the fundamental excitation frequency). Therefore, the estimation error θ_{err} is also expected to vary for different rotor positions at twice the fundamental excitation

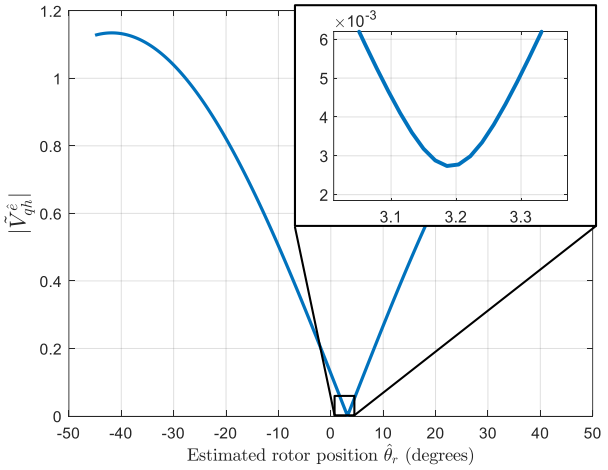

Fig. 6: Value of $|\tilde{\boldsymbol{V}}^{\hat{e}}_{qh}|$ for the investigated CSI drive calculated using (11) for different rotor position estimation values $\hat{\boldsymbol{\theta}}_r$ when the rotor is static at $\boldsymbol{\theta_r = 0}$.

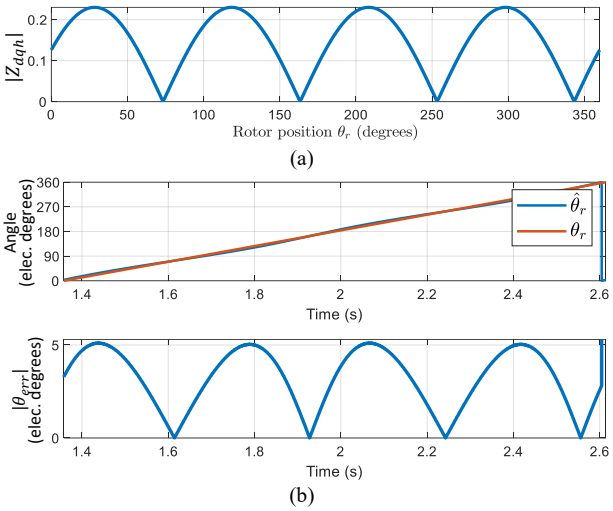

Fig. 7: (a) Calculated $|\boldsymbol{Z_{dqh}}|$ plotted vs. rotor position in the presence of unbalanced output capacitors; (b) simulation results of the PVE self-sensing method for unbalanced output capacitors plotted vs. time for one full electrical cycle.

frequency and to be correlated to the magnitude of $\boldsymbol{Z_{dqh}}$. Fig. 7(a) shows the calculated value of $|\boldsymbol{Z_{dqh}}|$ for different rotor positions, while Fig. 7(b) shows the simulation results of the PVE self-sensing algorithm for unbalanced output capacitors. By comparing Fig. 7(a) and Fig. 7(b), the strong correlation between $|\boldsymbol{Z_{dqh}}|$ and θ_{err} is clearly visible. It is important to mention that since Fig 7(a) and (b) plot the amplitude of $\boldsymbol{Z_{dqh}}$ and θ_{err} (without the corresponding phase) it may lead to a wrong impression that $\boldsymbol{Z_{dqh}}$ completes four full cycles (instead of two) within a single full rotor electrical cycle.

Note that increasing the frequency of the injected signal reduces the impedance values of the output filter capacitors while simultaneously increasing the machine inductance impedance, approaching the resonant frequency more closely. As a result, the effects of the capacitor unbalance become more prominent as the frequency increases. Fig. 8 shows simulation results of the PVE self-sensing method assuming the same unbalanced

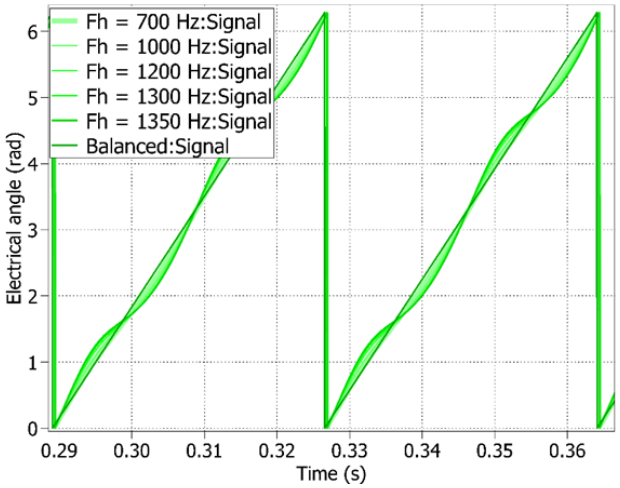

Fig. 8: Simulations of the PVE self-sensing method assuming unbalanced output capacitors ($\boldsymbol{C_a = 1.1C, C_b = C, C_c = 0.9C}$) for 5 different injected signal frequencies at 26.66 Hz electrical excitation frequency (400 rpm). The simulation waveform for balanced capacitors is included for reference comparison.

output capacitors ($C_a = 1.1\,C, C_b = C, C_c = 0.9\,C$) for 5 different injected signal frequencies for a low-speed excitation frequency of 26.66 Hz corresponding to 400 rpm. The results show that the estimation error oscillations grow in amplitude until it eventually becomes unstable as the injected signal frequency increases.

V. Experimental Verification of Unbalanced CSI Output Capacitor

This section presents experimental results for the analysis above. The experiments were conducted using a 3 kW CSI integrated motor drive. Fig. 9(a)-(g) present the assembled 3 kW CSI-IMD and its constituent parts, while Fig. 9(h) provides a simplified diagram of the entire system. The system consists of a CSR and a CSI arranged in a back-to-back configuration, as depicted in the power and sensor boards (refer to Fig. 9(c)-(d)). The controller TMS320F28379D is used to generate the gate signals and to implement the inverter control algorithm. It is important to mention that a data-logging capability was implemented in the controller allowing to collect simultaneously the estimated rotor position and the actual rotor position measured from a 12-bit incremental encoder at the sampling rate of 70 kHz (same rate of the control loop).

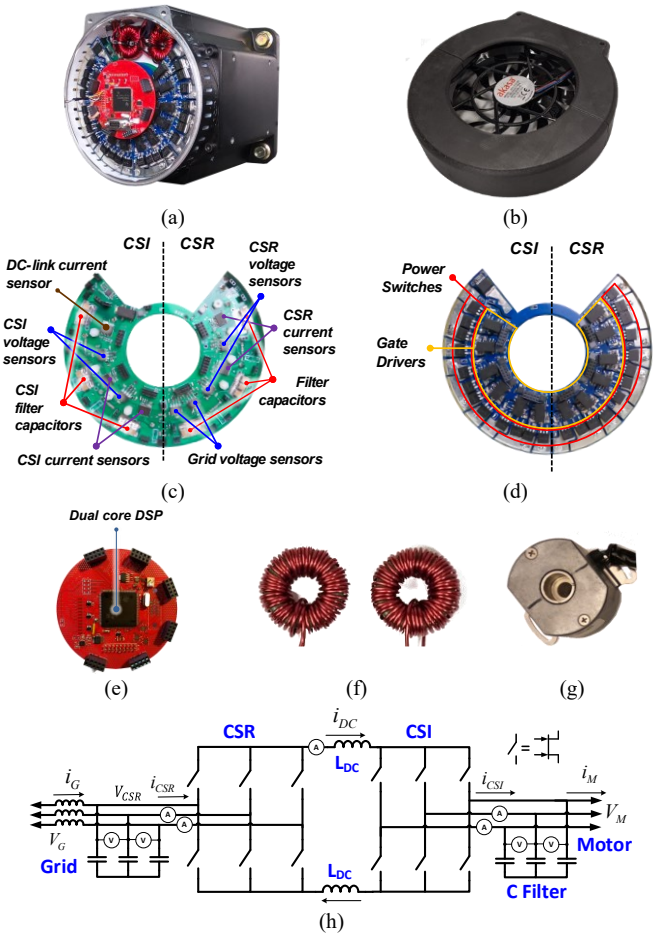

Fig. 9 Fully-assembled CSI-IMD and its components. (a) Fully assembled demonstrator with endcap removed; (b) Endcap with 3W integrated coolin fan; (c) Sensor board; (d) Power board; (e) Controller board; (f) DC-link inductors; (g) Incremental encoder; and (h) Simplified schematic of CSI-IM [21].

Fig. 10(a) and Fig. 10(b) compares the measured rotor position estimation using the PVE method for two different conditions: a) unbalanced output capacitors ($C_a = 1.1 \cdot 2.2\mu F, C_b = 2.2\mu F, C_c = 0.9 \cdot 2.2\mu F$); and b) balanced output capacitors ($C_a = C_b = C_c = 2.2\mu F$). For both conditions, the frequency of the high-frequency injected signal was varied from 600 Hz to 975 Hz, and the fundamental electrical frequency was held constant at 26.66 Hz, the same excitation frequency used for the simulation results in Fig. 8. Comparing Fig. 10(a) and Fig. 10(b) shows that unbalanced CSI output capacitors substantially degrade the performance of the PVE rotor position estimation, particularly at injection frequency values closer to the resonant frequency. This result is consistent with the trends exhibited by the analytical results in the preceding section. The rotor position estimation waveforms of Fig. 10(a) reflect the same type of angle-dependent behavior shown in Fig. 8, where the capacitor unbalance creates an oscillatory error with a frequency that is two times the fundamental excitation frequency. The experimental results in Fig. 10(a) also confirm the simulation results showing that the effects of the output capacitor unbalance become more prominent as the injection frequency increases.

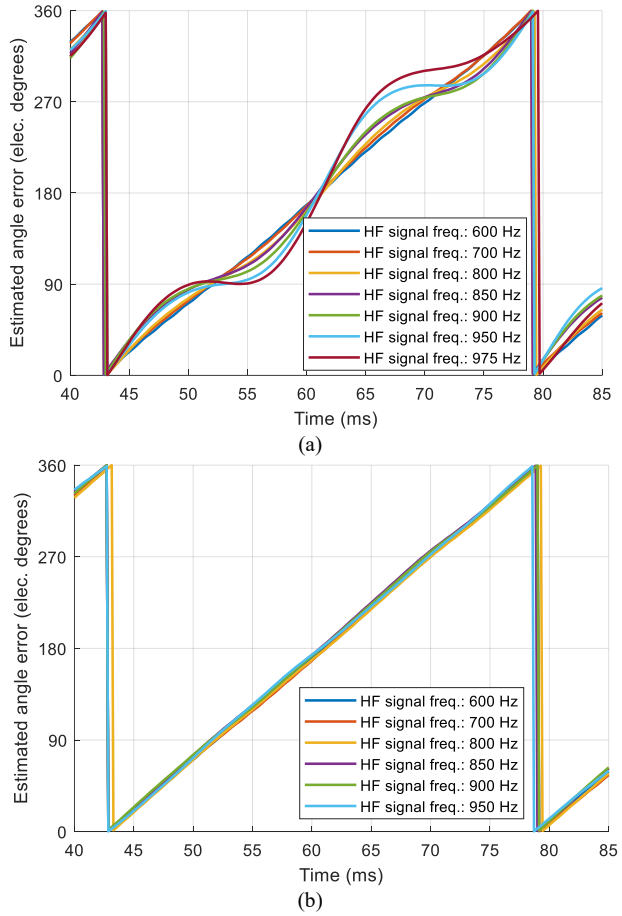

Fig. 10: Measured rotor position estimates using the PVE method under two different conditions: (a) unbalanced output capacitors ($\boldsymbol{C_a = 1.1 \cdot 2.2\mu F, C_b = 2.2\mu F, C_c = 0.9 \cdot 2.2\mu F}$); and (b) balanced output capacitors ($\boldsymbol{C_a = C_b = C_c = 2.2\mu F}$) at 26.66 Hz fundamental electrical frequency (400 RPM). The frequency of the high-frequency injected signal is varied from 600 Hz to 975 Hz.

The parameters and test conditions used for the simulation results in Fig. 8 were set to match those of the experimental results presented in Fig. 10(a) as closely as possible. However, the instability threshold of the PVE algorithm was reached during the experimental tests at a high-frequency injection frequency of approximately 1000 Hz which is noticeably lower than the 1300 Hz threshold frequency predicted by the simulation results. This difference could be caused by a variety of potential factors including parameter errors in the simulation, additional noise in the experiments, or higher unbalance in the capacitor values than expected. This last factor is a plausible contributor since the tolerance range of the capacitor values that were used during the experiments (KRM55TR73A224MH01K) is 20%.

VI. Conclusions

This paper has investigated the issue of tailoring the pulsating vector excitation saliency-based method for rotor position estimation of PM synchronous machines using CSI-based motor drives at static and low-speed operation. A detailed mathematical model for the rotor position estimation method has been provided, providing the analytical platform needed to investigate key implementation issues including the impact of capacitor unbalance and CSI-load resonance.

The paper has shown CSI's using WBG switches can provide an appealing environment for implementing self-sensing of rotor angular position based on high-frequency signal injection techniques using pulsating vector excitation. This investigation has demonstrated that the output filter capacitors of the CSI have implications for saliency-based rotor position estimation methods that provide both opportunities and challenges. First, the resonance circuit created by the output filter capacitance and the machine inductance can be used to amplify the HF injected signal, improving the SNR. On the other hand, injecting the HF signal close to the resonant frequency makes the rotor position estimation more sensitive to unbalanced output capacitor values.

A combination of analytical and experimental results has confirmed the importance of making a special effort to ensure that the filter capacitors are well-balanced; if not, the performance of the rotor position estimator can be seriously degraded, introducing serious errors into the angle estimates at two times the fundamental frequency.

The frequency of the injected signal can also play an important role in determining the performance of the position estimator, and the freedom to adjust its value dynamically during operation provides opportunities for optimizing its value that extend beyond the scope of this paper. More of these issues related to the extraction of maximum performance from self-sensing rotor position estimation techniques in CSI-based motor drives will be addressed in future publications.

Acknoledgements

The information, data, or work presented herein was funded in part by the Advanced Research Projects Agency-

Energy (ARPA-E), U.S. Department of Energy, under Award Number DE-AR0000893. The views and opinions of authors expressed herein do not necessarily state or reflect those of the United States Government or any agency thereof. The authors also gratefully acknowledge the support of the Wisconsin Electric Machines and Power Electronics Consortium (WEMPEC), including access to its laboratory facilities.

REFERENCES

[1] B. Brusso and B. Bose, "Power electronics: Historical perspective and my experience [history]," *IEEE Ind. Appl. Mag.*, vol. 20, no. 2, pp. 7–14, 2014.

[2] B. J. Baliga, D. Hopkins, S. Bhattacharya, A. Agarwal, T.-H. Cheng, R. Narwal, A. Kanale, S. S. Shah, and K. Han, "The BiDFET device and its impact on converters," *IEEE Power Electron. Mag.*, vol. 10, no. 1, pp. 20–27, Mar. 2023.

[3] V. Madonna, G. Migliazza, P. Giangrande, E. Lorenzani, G. Buticchi, and M. Galea, "The Rebirth of the Current Source Inverter: Advantages for Aerospace Motor Design," *IEEE Ind. Electron. Mag.*, vol. 13, no. 4, pp. 65–76, 2019.

[4] R. A. Torres, H. Dai, W. Lee, T. M. Jahns, and B. Sarlioglu, "Evaluation of sensorless techniques for surface permanent-magnet integrated motor drive using current-source inverter," in *Proc. IEEE Energy Conversion Congress and Exposition (ECCE)*, 2020, pp. 2387–2394.

[5] Joong-Ho Song, Kwang-Bae Kim, and Myung-Joong Youn, "Eigenvalue sensitivity of a speed-sensorless CSI-fed induction motor system," in *Proc. IECON '93 - 19th Annual Conference of IEEE Industrial Electronics*, 1993, pp. 987–991.

[6] J. Hu and B. Wu, "Field oriented control CSI synchronous motor drive without shaft sensors," in *Proc. Proceedings of the International Conference on Power Electronics and Drive Systems*, 1997, vol. 2, no. 2, pp. 798–803.

[7] H. Feroura, F. Krim, B. Talbi, A. Laib, and A. Belaout, "Sensorless field oriented control of current source inverter fed induction motor drive," *Rev. Roum. des Sci. Tech. Ser. Electrotech. Energ.*, vol. 63, no. 1, pp. 100–105, 2018.

[8] Q. Song, Z. Wang, P. Liu, Y. Xu, C. Tang, and M. Cheng, "Sensorless control of current-source-converters fed synchronous motor drives using high frequency signal injection," in *Proc. International Conference on Electrical Machines and Systems (ICEMS)*, 2019, pp. 1–5.

[9] M. Morawiec and F. Wilczynski, "Sensorless control of five-phase machine supplied by the current source inverter," in *Proc. International Conference on Electrical Power Drive Systems (ICEPDS)*, 2020, pp. 1–6.

[10] A. Nikolic and B. Jeftenic, "Speed sensorless direct torque control implementation in a current source inverter fed induction motor drive," in *Proc. IEEE 35th Annual Power Electronics Specialists Conference*, 2004, pp. 2843–2848.

[11] M. Meiqin, L. Fuyan, M. Junsheng, and X. Bin, "Sensorless control of PMSG for a wind power system based on CSC," in *Proc. 8th International Conference on Power Electronics - ECCE Asia*, 2011, no. 1, pp. 2175–2179.

[12] Z. Wang, Y. Zheng, Z. Zou, and M. Cheng, "Position sensorless control of interleaved CSI fed PMSM drive with extended kalman filter," *IEEE Trans. Magn.*, vol. 48, no. 11, pp. 3688–3691, Nov. 2012.

[13] A. K. Abdelsalam, M. I. Masoud, M. S. Hamad, and B. W. Williams, "Improved sensorless operation of a CSI-based induction motor drive: long feeder case," *IEEE Trans. Power Electron.*, vol. 28, no. 8, pp. 4001–4012, Aug. 2013.

[14] E. Al-nabi, B. Wu, N. R. Zargari, and V. Sood, "Sensorless control of CSC-fed IPM machine for zero- and low-speed operations using pulsating HFI method," *IEEE Trans. Ind. Electron.*, vol. 60, no. 5, pp. 1711–1723, May 2013.

[15] H. C. Chen and H. H. Huang, "Design of buck-type current source inverter fed brushless DC motor drive and its application to position sensorless control with square-wave current," *IET Electr. Power Appl.*, vol. 7, no. 5, pp. 416–426, 2013.

[16] P. D. Jyothsna and S. Harinath, "Sensor less Operation of CSI Fed Induction Motor Drive by Using MRAS," *IOSR J. Electr. Electron. Eng.*, vol. 9, no. 6, pp. 01–06, 2014.

[17] M. Morawiec, "Sensorless control of induction machine supplied by current source inverter," *Asian J. Control*, vol. 17, no. 6, pp. 2403–2408, Nov. 2015.

[18] Ji-Hoon Jang, S.-K. Sul, Jung-Ik Ha, K. Ide, and M. Sawamura, "Sensorless drive of surface-mounted permanent-magnet motor by high-frequency signal injection based on magnetic saliency," *IEEE Trans. Ind. Appl.*, vol. 39, no. 4, pp. 1031–1039, Jul. 2003.

[19] E. Al-nabi, "Sensorless current source-fed PM drive system for low speed operations," Ryerson University, 2013.

[20] Y. Li, Z. Q. Zhu, D. Howe, C. M. Bingham, and D. A. Stone, "Improved rotor-position estimation by signal injection in brushless AC motors, accounting for cross-coupling magnetic saturation," *IEEE Trans. Ind. Appl.*, vol. 45, no. 5, pp. 1843–1850, 2009.

[21] R. Amorim Torres, H. Dai, W. Lee, B. Sarlioglu, and T. Jahns, "Current-Source Inverter Integrated Motor Drives Using Dual-Gate Four-Quadrant Wide-Bandgap Power Switches," *IEEE Trans. Ind. Appl.*, vol. 57, no. 5, pp. 5183–5198, 2021.